The Astrophysical Journal, 943:169 (15pp), 2023 February 1 https://doi.org/10.3847/1538-4357/acaf52

Quasi-parallel Whistler Waves and Their Interaction with Resonant Electrons during High-velocity Bulk Flows in the Earth's Magnetotail

Elena E. Grigorenko[1], Andrey Y. Malykhin[1], Elena A. Kronberg[2], and Evgeny V. Panov[3]
[1] Space Research Institute of RAS, Moscow, Russia; elenagrigorenko2003@yandex.ru
[2] Department of Earth and Environmental Sciences, Ludwig Maximilian University of Munich, Munich, Germany
[3] Space Research Institute, Austrian Academy of Sciences, Graz, Austria
Received 2022 November 21; revised 2022 December 23; accepted 2022 December 28; published 2023 February 7

Abstract

In collisionless space, plasma waves are important channels of energy conversion, affecting the local particle velocity distribution functions through wave–particle interactions. In this paper we present a comparative statistical analysis of the characteristics of quasi-parallel narrowband whistler waves and the properties of resonant electrons interacting with these waves during the intervals of earthward and tailward high-velocity bulk flows produced by the near-Earth X-line and observed by Magnetospheric Multiscale Mission spacecraft. We found that on both sides of the X-line, the suprathermal electrons ($\geqslant$1 keV) having large pitch angles make the major contribution to the maximal growth rate (γ) of these waves. The whistler waves were observed almost simultaneously with strong enhancements of perpendicular magnetic gradients localized at electron scales near dipolarization fronts associated with the earthward bulk flows, and near flux ropes/magnetic islands embedded into the tailward bulk flows. Betatron energization of electrons due to the appearance of such gradients increases the perpendicular anisotropy of electron distribution, which could be responsible for the whistler wave generation. We found that in the course of electron interactions with the whistler waves the lower-energy resonant electrons can transfer a part of their kinetic energy to the higher-energy electrons, especially in the Central Plasma Sheet. This results in formation/enhancement of energy-dependent perpendicular anisotropy and power-law tails in the high-energy range of electron velocity distribution. We conclude that despite the differences in the magnetic structure of the earthward and tailward bulk flows, the mechanisms of the quasi-parallel whistler wave generation and the properties of resonant electrons are quite similar.

Unified Astronomy Thesaurus concepts: Planetary magnetospheres (997); Space plasmas (1544)

1. Introduction

High-velocity bulk flows produced by magnetic reconnection transport energy and mass in the opposite directions from the magnetotail X-line. Being important energy sources, the high-velocity bulk flows play a significant role in the magnetotail dynamics evolved at various spatial and temporal scales. This includes substorm development (e.g., Fairfield et al. 1999; Sergeev et al. 2012; Merkin et al. 2019), current sheet (CS) perturbations (e.g., Sergeev et al. 2004; Grigorenko et al. 2014), generation of wave activity, and wave–particle interactions (e.g., Liang et al. 2012; Zhang & Angelopoulos 2014).

The observed direction of a bulk flow (earthward/tailward) depends on the spacecraft location relative to the X-line (e.g., Hones 1977; Runov et al. 2003). In the near-Earth tail ($X > -20\ R_E$), the earthward flows dominate indicating on the magnetic reconnection occurrence downtail (e.g., Baumjohann et al. 1990; Angelopoulos et al. 1992). Farther downtail ($X < -20\ R_E$), the fraction of tailward bulk flows increases (e.g., Angelopoulos et al. 1994; Nagai et al. 1998), and at ARTEMIS location ($X \sim -60\ R_E$), approximately half of the observed bulk flows are directed tailward (e.g., Kiehas et al. 2018). These results show that quite often a magnetic X-line is formed in $-60\ R_E < X < -20\ R_E$, and sometimes even closer to the Earth (e.g., Borg et al. 2005).

Magnetospheric Multiscale Mission (MMS) with its apogee at $X \sim -25\ R_E$ in the magnetotail is appropriate to study the plasma processes on both sides of a near-Earth X-line (Burch et al. 2016). Although the earthward and tailward high-velocity bulk flows are considered to be the manifestations of the same reconnection process, their magnetic structures and plasma characteristics are quite different. Namely, dipolarization fronts (DFs) or dipolarizing flux bundles (DFBs) are usually associated with the earthward bulk flows. Such magnetic structures manifest in a sharp and strong increase in the northward (B_Z) component of the magnetic field, which is preceded by relatively small negative B_Z excursion (e.g., Ohtani et al. 1992; Nakamura et al. 2002; Shiokawa et al. 2005; Runov et al. 2009; Liu et al. 2014; Fu et al. 2020). During the tailward bulk flows, various types of the magnetic structures were reported: plasmoids, flux ropes/magnetic islands with bipolar B_Z variations and the enhanced core field (B_Y) (e.g., Slavin et al. 2003; Drake et al. 2006; Zhao et al. 2016; Sun et al. 2019), and antidipolarization fronts (ADFs) with a strong negative pulse of B_Z field (e.g., Li et al. 2014).

Multipoint spacecraft observations showed that the magnetic structures associated with the earthward and tailward bulk flows can be formed at ion and sub-ion kinetic scales and/or have very thin fronts/boundaries with a characteristic thickness of the order of ion gyroradius or less (Sergeev et al. 2009; Balikhin et al. 2014; Huang et al. 2016; Grigorenko et al. 2018; He et al. 2021). These structures can be the sites of strong energy dissipation (e.g., Drake et al. 2006; Fu et al. 2006; Oka et al. 2010; Huang et al. 2019), which affects the particle velocity distribution functions and causes the generation of

various types of electromagnetic and electrostatic wave modes (e.g., Zhang et al. 1999; Le Contel et al. 2009; Tenerani et al. 2013; Fujimoto 2014, 2017; Zhang & Angelopoulos 2014; Grigorenko et al. 2016; Huang et al. 2016; Wang et al. 2016; Guo et al. 2021; Pickett 2021).

Processes of wave–particle interactions are important tools of energy conversion, especially in the collisionless plasma. Whistler waves are one of the widely observed wave modes in space plasma. Observations of whistler waves were reported in planetary magnetospheres and in the solar wind (e.g., Thorne & Tsurutani 1981; Wei et al. 2007; Lacombe et al. 2014; Tong et al. 2019; Vasko et al. 2019). In the Earth's magnetotail, many spacecraft missions observed whistler waves around the DFs/DFBs associated with the earthward bulk flows (e.g., Le Contel et al. 2009; Viberg et al. 2014; Breuillard et al. 2016; Zhang et al. 2018). It was shown that these waves play an important role in energy transport and electron energization and scattering, as well as in electron anisotropy buildup and relaxation (e.g., Panov et al. 2013; Liu & Fu 2019; Zhang et al. 2019; Grigorenko et al. 2020; Artemyev et al. 2022). It was also shown that the perpendicular anisotropy of electron velocity distribution function formed by the betatron acceleration in DFs/DFBs is a source of quasi-parallel whistler waves (e.g., Khotyaintsev et al. 2011; Zhang et al. 2018; Malykhin et al. 2021). The excited waves, while propagating from the source, interact with the resonant electrons and serve as conduits for energy transfer between different parts of electron distribution function (e.g., Shklyar 2011, 2017; Grigorenko et al. 2020; Malykhin et al. 2021). This can lead to electron energization in a finite energy range (e.g., Liu & Fu 2019; Zhao et al. 2019). MMS observations showed that in the DFs/DFBs associated with the earthward bulk flow, the resonant electrons have energies >1 keV, so that the electron interaction with the whistler waves may significantly affect the velocity distribution function and its anisotropy in suprathermal energy range (e.g., Grigorenko et al. 2020; Malykhin et al. 2021).

Tailward bulk flows transport energy and mass downtail from a reconnection region. Whereas the earthward bulk flows are decelerated by the stronger magnetic field as they approach the near-Earth region, the tailward bulk flows usually do not experience such deceleration, especially once reconnection reaches the lobe magnetic field. This may explain the differences in magnetic and plasma characteristics observed in the earthward and tailward bulk flows. These differences may affect the mechanisms of wave generation, the processes of wave–particle interaction, and the characteristics of resonant plasma particles interacting with a particular wave mode during earthward and tailward bulk flows.

Our paper is aimed to compare statistically the occurrence frequency and characteristics of whistler waves as well as peculiarities of their interaction with resonant electrons during earthward and tailward bulk flows, i.e., on earthward and tailward sides of a near-Earth X-line. In Section 2 we present two typical examples of quasi-parallel whistler wave observations during earthward and tailward bulk flows. The analysis presented in Section 2 has been applied to all intervals of the bulk flows from our database in order to obtain the statistical results presented in Section 3 and discussed in Section 4.

2. Observations

For the analysis of whistler waves' interaction with resonant electrons, we use the burst mode observations from the MMS Mission (Burch et al. 2016); 3D electron velocity distribution functions measured in the energy range from ~10 eV to 30 keV with 30 ms time resolution are provided by the FPI instrument (Pollock et al. 2016). The magnetic field observations are provided by the fluxgate magnetometer (Russell et al. 2016) and by search coil magnetometer (Le Contel et al. 2016).

The geocentric solar magnetospheric (GSM) coordinate system is used everywhere in the paper.

2.1. Whistler Wave Observations during Tailward and Earthward Bulk Flows

On 2019 September 9 at 01:16:00–01:18:40 UT, MMS spacecraft were located in the northern part of the Plasma Sheet (PS) at [−25, 13, 1] R_E. Figure 1 shows an overview of MMS-1 observations for this interval. The observations from the other probes are similar and not shown.

A high-velocity bulk flow moving tailward with $V_X \sim -600$ km s^{-1} started around 01:16:10 UT and was observed until the end of the interval of interest (see Figure 1(a)). This means that at this time the MMS spacecraft were located tailward of a near-Earth X-line (e.g., Runov et al. 2003). During the interval of interest MMS experienced a couple of excursions to the neutral plane and observed three bipolar variations of B_Z component of the magnetic field. The first one was registered between ~01:16:40 and ~01:17:10 UT along with the strong negative B_Y variation (see Figure 1(b)). The second and third weak bipolar variations of B_Z field were observed at ~01:18:10–01:18:18 UT and at ~01:18:18–01:18:25 UT also along with some negative B_Y variations. The bipolar B_Z variations and the enhancement of $|B_Y|$ field may be related to flux ropes propagation (e.g., Slavin et al. 2003).

Three bursts of whistler waves were detected at ~01:16:17–01:16:38 UT, at ~01:17:32–01:17:35 UT, and at 01:18:22–01:18:30 UT (Figure 1(e), (f)). These intervals are marked by the solid lines and denoted by "I," "II," and "III," respectively. The first burst (I) of whistler waves was observed at the beginning of the bulk flow and near the leading edge of the first flux rope, when MMS spacecraft were in the PS ($B_X \sim$ 7 nT). The second burst (II) was detected in the flow maximum and near the trailing edge of the first flux rope, when MMS spacecraft were located near the neutral plane ($B_X \sim 3$ nT). The third burst (III) was observed in the end of the bulk flow and inside the third flux rope, when MMS spacecraft were moving to the outer part of the PS ($B_X \geqslant 10$ nT). The whistler waves have small wave normal angles (<30°, see Figure 1(c)) and right-hand polarization (the ellipticity is close to 1, see Figure 1(d)) and are characterized by a high degree of polarization (close to 1, see Figure 1(g)).

In the right part of the figure we present the frequency spectra of the power spectral density (PSD) of the magnetic field fluctuations observed at the beginning, in the middle, and at the end of whistler burst II (Figure 1(j)–(l), respectively). The red color marks the segments of the spectra at which the wave normal angle was less than 40°, and polarization and ellipticity were larger than 0.7. The red segments correspond to the bulge in frequency spectra observed in a limited frequency range. This means that the whistler waves with right-hand polarization propagate in the quasi-parallel direction relatively to the ambient magnetic field and represent narrowband wave bursts. These characteristics of the whistler waves are similar to those observed at and behind the DFs on the earthward side of the X-line by different spacecraft missions (e.g.,

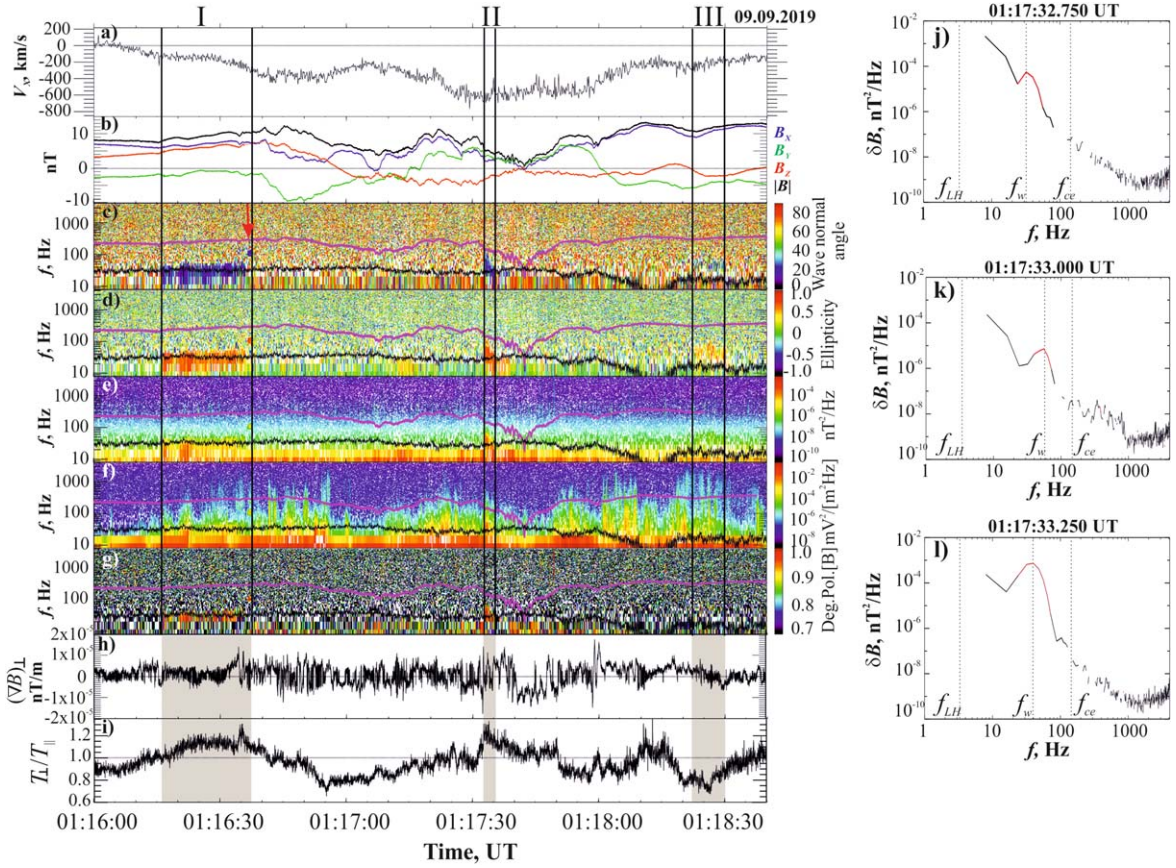

Figure 1. An example of quasi-parallel whistler wave observations by MMS-1 during tailward bulk flow on 2019 September 9. (a): the time profile of ion bulk velocity V_X; (b): three components of the magnetic field and $|B|$; (c): frequency–time (F–T) spectrogram of wave normal angle; (d): F–T spectrogram of ellipticity; (e): F–T spectrogram of the power spectral density (PSD) of magnetic field; (f): spectrogram of the PSD of electric field; (g): degree of polarization; (h): perpendicular component of the magnetic field gradient; (i): electron $\frac{T_\perp}{T_\parallel}$. Three whistler bursts intervals ("I," "II," and "III") are marked by the vertical solid lines and shaded by gray color. The solid magenta and black lines in panels (c)–(g) display the time profiles of electron gyrofrequency (f_{ce}) and proton plasma frequency (f_{pp}), respectively. (j)–(l): Frequency spectra of the PSD of magnetic field measured during whistler burst "II."

Le Contel et al. 2009; Huang et al. 2012; Grigorenko et al. 2020; Malykhin et al. 2021).

For each moment within the whistler burst we determine the frequency of the whistler wave f_w as the frequency corresponding to the maximum of the PSD of the magnetic fluctuations located within the red segment of the spectrum (the value of f_w is displayed in the horizontal axis in Figure 1(j)–(l) along with the local low-hybrid frequency, $f_{\rm LH}$, and electron gyrofrequency, f_{ce}). In the beginning of the whistler burst, $f_w \sim 32$ Hz $\sim 0.2 f_{ce}$ (Figure 1(j)). Then f_w increases to $\sim$58 Hz $\sim 0.4_{ce}$ (Figure 1(k)), and by the end of the whistler burst, f_w decreases again to $\sim$35 Hz $\sim 0.2 f_{ce}$ (Figure 1(l)).

Figure 1(i) presents the time profile of electron temperature anisotropy $\frac{T_\perp}{T_\parallel}$. The bursts I and II are observed simultaneously with the perpendicular temperature anisotropy $\frac{T_\perp}{T_\parallel} > 1$. It is worth noting that a sharp increase in $\frac{T_\perp}{T_\parallel}$ observed at the end of burst I occurs almost simultaneously with the sharp increase in whistler wave frequency (this moment is marked by the red arrow in Figure 1(c)). Similarly, during whistler burst II the perpendicular anisotropy of electrons increases at first, and then it decreases by the end of the burst. The variation in $\frac{T_\perp}{T_\parallel}$ corresponds to the changes in whistler wave frequency, which also increases in the beginning of the burst and decreases by the end of the burst. This behavior is in agreement with the condition of electron cyclotron instability: $\frac{f_w}{f_{ce}} \leqslant \frac{T_\perp - T_\parallel}{T_\perp}$ (Trakhtengerts & Rycroft 2008).

Figure 1(h) shows the time profile of the perpendicular $(\nabla B)_\perp$ magnetic gradient. The magnetic gradient vector was calculated from four-point MMS measurements of the magnetic field by using curlometer technique (Robert et al. 1998). To show whether the variations of $(\nabla B)_\perp$ are positive or negative, we first determine which component of the perpendicular magnetic gradient vector $(\nabla B)_{\perp_i}$ makes the main contribution to its absolute value at each moment during the interval of interest (here i is one of three GSM components of the perpendicular magnetic gradient vector). Then, at each moment we calculate the value of $(\nabla B)_\perp$ as $|(\nabla B)_\perp| \cdot \frac{(\nabla B)_{\perp_i}}{|(\nabla B)_{\perp_i}|}$. Transient positive increases in $(\nabla B)_\perp$ ($>0.5 \times 10^{-5}$ nT m^{-1}) are observed just before and near the end of bursts I and II. We speculate that the local increase in $(\nabla B)_\perp$ causes the increase in electron perpendicular anisotropy, which in turn can be a source of the observed quasi-parallel whistler waves.

However, burst III is observed along with the decrease in $(\nabla B)_\perp$. Also the negative variation of $(\nabla B)_\perp$ is detected at the end of the burst. Such behavior of the magnetic gradient may cause particle deceleration and a decrease in electron perpendicular anisotropy. Indeed, during burst III the increase in parallel electron temperature anisotropy is observed ($\frac{T_\perp}{T_\parallel} < 1$). We suggest that this whistler burst was not generated locally

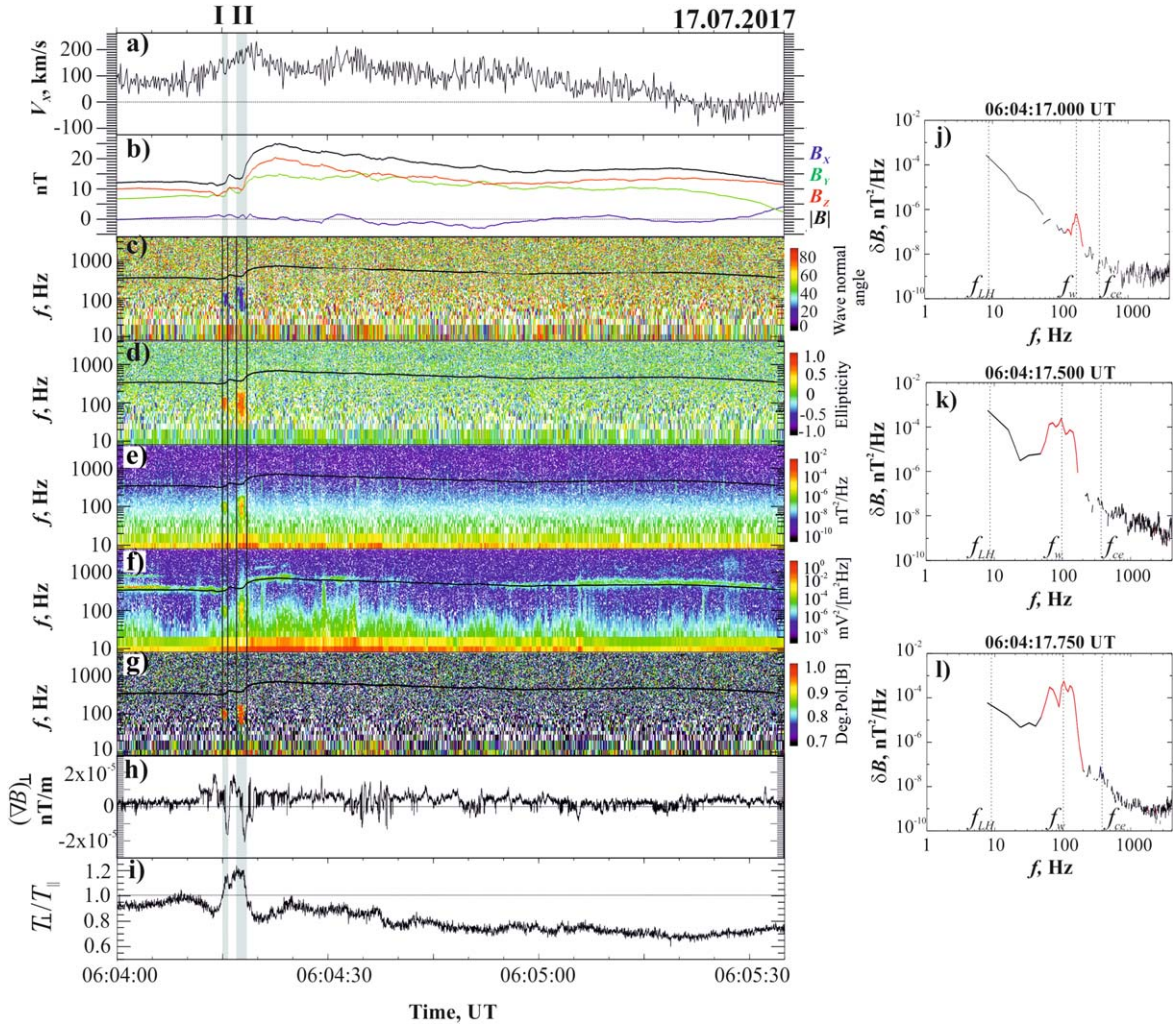

Figure 2. An example of quasi-parallel whistler wave observations by MMS-1 during earthward bulk flow on 2017 July 17. The solid black line in panels (c)–(g) shows the time profile of f_{ce}. The format of the figure is the same as that of Figure 1.

but propagated to the MMS spacecraft from a remote source. This fact is also consistent with the weaker PSD of magnetic fluctuations in burst III as compared with bursts I and II.

Figure 2 presents an overview of the whistler wave observations by MMS-1 during the earthward bulk flow observed on 2017 July 17 at 06:04:00–06:05:35 UT. The observations from the other probes are similar and not shown. The format of the figure is the same as the format of the Figure 1.

At this time MMS spacecraft were located near the neutral plane of the magnetotail current sheet (CS) at $[-17, 7, 1]\ R_E$. A bulk flow moving earthward with $V_X \sim 200$ km s^{-1} started at ~06:04:10 UT (Figure 2(a)). A sudden increase in the northward B_Z field up to ~25 nT was observed almost simultaneously with V_X maximum denoting the arrival of the DF (e.g., Runov et al. 2009). Two small negative variations of B_Z were observed before the DF (Figure 2(b)) simultaneously with the decrease in $|B|$ (so-called magnetic dip, e.g., Shiokawa et al. 2005). Within the intervals of the magnetic dips two bursts of quasi-parallel whistler waves were observed (see Figure 2(c)–(g)). In Figure 2 these intervals are marked as "I" and "II." The characteristics of these waves are similar to those observed during the tailward bulk flow and discussed above.

In the right part of Figure 2, the frequency spectra of the PSD of magnetic field fluctuations observed at the beginning, in the middle, and at the end of whistler burst II are shown (see Figure 2(j)–(l), respectively). The red color marks the segments of the spectra at which the wave normal angle was less than 40°, and polarization and ellipticity were larger than 0.7. It is seen that similarly to the previous event, the quasi-parallel whistler waves were narrowband. In the beginning of the whistler burst, $f_w \sim 170$ Hz $\sim 0.45 f_{ce}$ (Figure 2(j)). Then f_w decreases to ~98 Hz $\sim 0.25 f_{ce}$ (Figure 2(k)), and by the end of the whistler burst, f_w becomes ~102 Hz $\sim 0.27 f_{ce}$ (Figure 2(l)).

Figure 2(i) presents the time profile of electron temperature anisotropy $\frac{T_\perp}{T_\parallel}$. Each whistler burst was observed simultaneously with the local increase in $\frac{T_\perp}{T_\parallel}$ followed by its relaxation at the end of the burst. Figure 2(h) shows the time profile of $(\nabla B)_\perp$ calculated in the way described above. Strong transient bipolar variations of $(\nabla B)_\perp$ ($>1 \times 10^{-5}$ nT m^{-1}) were observed during and around the bursts.

We suggest that the local positive variations in the perpendicular magnetic gradient observed at electron scales can cause the observed increase in electron perpendicular anisotropy, which in turn can be the source of quasi-parallel whistler waves. In the next subsection we discuss the

characteristics of resonant electrons interacting with the whistler waves in these events and the peculiarities of energy exchange between different populations of the resonant electrons through their interactions with the waves.

2.2. The Definition of Energies and Pitch Angles of Resonant Electrons

High-resolution MMS observations of 3D electron velocity distribution function make it possible to calculate the growth rate, γ, and analyze its dynamics at the short timescale of a whistler burst (~a few seconds or less). General expression for linear growth rate of quasi-parallel whistler waves has been obtained by Sagdeev & Shafranov (1961) and Trakhtengerts & Rycroft (2008). We calculate γ from the observed local electron velocity distribution function, taking into account that only the first cyclotron resonance $n = 1$ is the most important for the quasi-parallel wave propagation (e.g., Shklyar & Matsumoto 2009). The details of this calculation are described in Grigorenko et al. (2020).

For the first cyclotron resonance, the parallel energy of resonant electrons, $W_{||\_res}$, can be calculated using the dispersion relation for quasi-parallel whistler waves:

$$W_{||\_res} = m_e c^2 \frac{(f_{ce} - f_w)^3}{2 f_w f_{pe}^2} \quad (1)$$

where m_e is the mass of electron and c is the speed of light.

It is worth noting that electrons moving in a given direction with respect to the ambient magnetic field (either parallel or antiparallel) amplify waves propagating in the opposite direction (i.e., antiparallel or parallel, respectively).

To define the total energy, W_{res}, and pitch angles, α_{res}, of the resonant electrons, we calculate γ as a function of wave frequency at each moment within each whistler burst. Also, at each moment we calculate the contribution to γ made by electrons with perpendicular energy, $W_\perp$ at fixed $W_{||\_res}$ (for details see Grigorenko et al. 2020). We will use this characteristic for the analysis of energy exchange between the waves and resonant electrons of different energies.

Before analyzing the characteristics of resonant electrons and their energy exchange with the waves, we select those moments during the whistler bursts when the frequency of the most unstable wave, f_γ (i.e., the frequency corresponding to the maximum of γ), was almost equal to the observed wave frequency, f_w:

$$\frac{|f_w - f_\gamma|}{f_w} \leqslant 0.2. \quad (2)$$

At such moments the anisotropy of local electron velocity distribution function could be responsible for the generation of whistler waves with the observed frequency, f_w; i.e., the wave source can be located close to the spacecraft. At such moments we determine the energies and pitch angles of resonant electrons as well as their contributions to γ.

In Figure 3 we present the time profiles of the power of magnetic field fluctuations, δB (Figure 3(b)), $f_w(t)$, and $f_\gamma(t)$ (shown by the black and red dots in Figure 3(c), respectively), for the tailward bulk flow event on 2019 September 9 at 01:16:00–01:18:40 UT. Figure 3(d) shows the color-coded energy–time spectrogram of the ratio of the perpendicular electron flux to the parallel electron flux ($F_\perp/F_\parallel$). As the $F_{||}$ value, we used either the flux of electrons moving with pitch angles near 0° or the flux of electrons with pitch angles near 180°, depending on which flux was larger. In Figure 3(d) we also show the time profile of $W_{||\_res}$ displayed by black dots.

The energy-dependent perpendicular anisotropy of electron flux ($\frac{F_\perp}{F_\parallel} > 1$) was observed in the suprathermal energy range (>1 keV) from ~3 s after the beginning of burst I and to the end of this burst. It also was observed during the entire interval of burst II. Simultaneously, the increase in perpendicular temperature anisotropy ($\frac{T_\perp}{T_\parallel}$) was also detected (see Figure 3(e)). During these intervals the condition (2) was fulfilled, i.e., $f_w \sim f_\gamma$. This means that at this time the observed whistler waves can be generated due to the local anisotropy of electron velocity distribution function in the suprathermal energy range. Indeed, the values of $W_{||\_res}$ were inside the energy range at which $\frac{F_\perp}{F_\parallel} > 1$ (see Figure 3(d)). Thus, at this time the source of whistler waves can be located close to the spacecraft.

During burst III, the perpendicular anisotropy of electron flux was not observed and the electron temperature anisotropy was parallel ($\frac{T_\perp}{T_\parallel} < 0$). From Figure 3(d) it is seen that at this time the parallel energies of resonant electrons were close or even exceeded the high-energy threshold of the FPI instrument. In such a case, the value of $\frac{T_\perp}{T_\parallel}$ measured by FPI does not show the real anisotropy of the high-energy resonant electron population. It is worth noting also that during burst III, the condition (2) was fulfilled during only a short time interval in the middle of the burst. Thus, we suggest that during a major part of this burst the observed whistler waves either could be generated in a remote source, or the mechanism of their generation is not related to the excitation of electron cyclotron instability.

Figure 3(f) and (g) show the values of total energies $W_{res} = W_\perp + W_{||\_res}$ and pitch angles of resonant electrons that make the maximal positive ($W+$, $\alpha+$, shown by the red dots) and the strongest negative ($W-$, $\alpha-$, shown by the black dots) contributions to γ at each moment of time during each burst. The resonant electrons that make the positive contribution to γ lose their energy by transferring it to the wave, and thus could be responsible for the wave generation. In contrast, the negative contribution to γ means that such resonant particles obtain the energy from the wave and increase their perpendicular anisotropy. Thus, there is an energy exchange between different populations of resonant electrons through their interactions with the whistler waves.

During the major part of burst I and during burst III, the total energies of resonant electrons making as positive ($W+$) as the negative ($W-$) contributions to γ were larger than 10 keV. During burst II, the total energies of resonant electrons were lower ~1–8 keV. During all bursts, electrons making the maximal positive contribution to γ had pitch angles ($\alpha+$) in the range of ~50°–80° and ~100°–140° for the waves with $\boldsymbol{k} \cdot \boldsymbol{B} < 0$ and $\boldsymbol{k} \cdot \boldsymbol{B} > 0$, respectively ($\boldsymbol{k}$ is the wavevector). Electrons making the main negative contribution to γ at each moment were more field-aligned, and their pitch angles were $\alpha- \sim 40°$–70° and 110°–150° for the waves with $\boldsymbol{k} \cdot \boldsymbol{B} < 0$ and $\boldsymbol{k} \cdot \boldsymbol{B} > 0$, respectively.

At some moments during the bursts, the value of $W-$ was larger than $W+$. This means that at these moments electrons with lower energies transferred a part of their kinetic energy to the wave, while the higher-energy electrons absorbed the

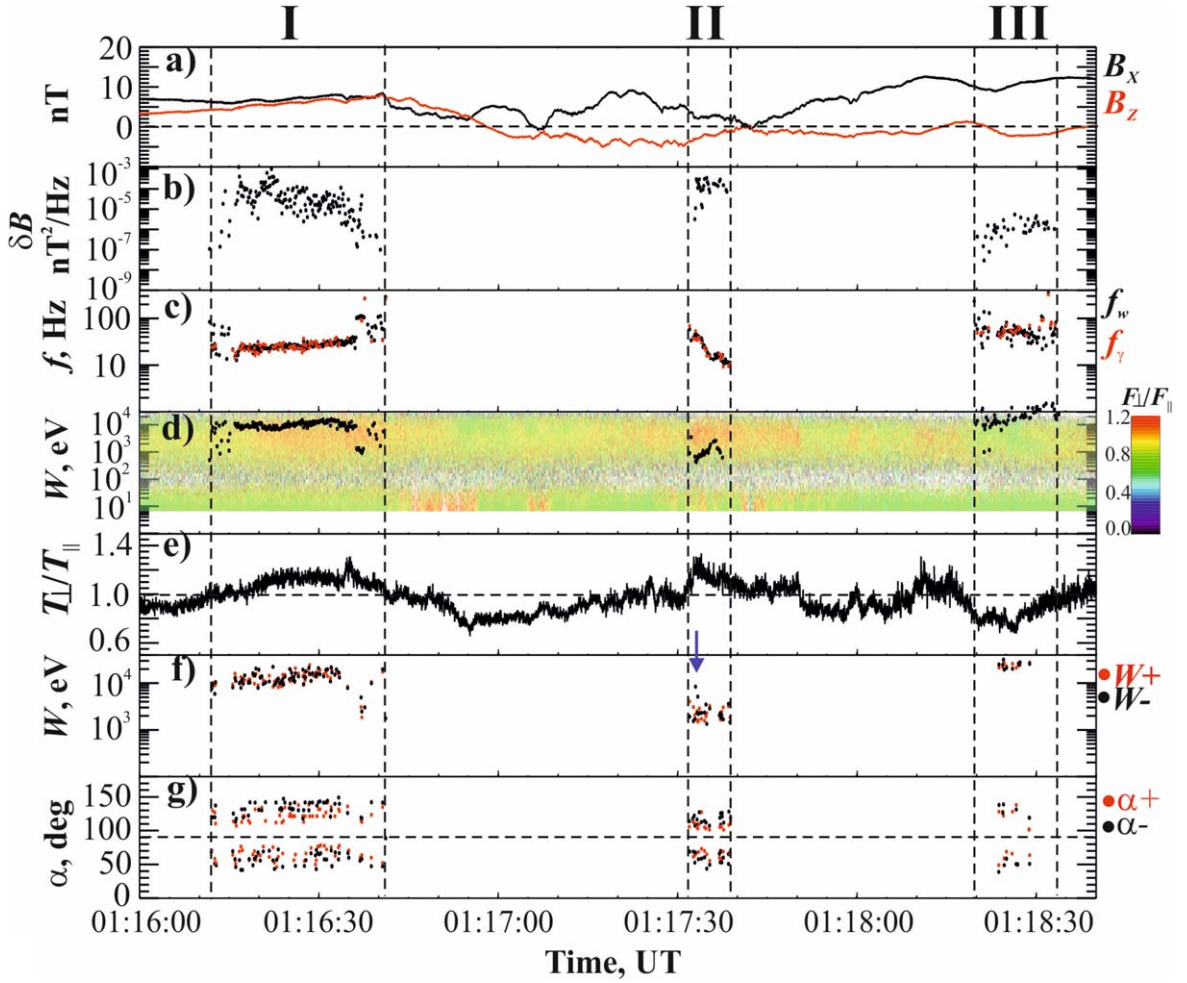

Figure 3. MMS-1 observations on 2019 September 9. (a): the time profiles of B_X and B_Z field; (b): the PSD of the magnetic field fluctuations corresponding to the whistler bursts marked as "I"–"III" in Figure 1; (c): frequency of narrowband whistler waves, f_w (black dots), and frequency corresponding to the maximal γ, f_γ (red dots); (d): color-coded energy–time distribution of electron $\frac{F_\perp}{F_\parallel}$. The black dots mark $W_{\parallel\_res}$; (e): time profile of $\frac{T_\perp}{T_\parallel}$; (f): total energies $W+$ (red dots) and $W-$ (black dots) of resonant electrons making maximal positive and main negative contributions to γ, respectively; (g): pitch angles $\alpha+$ (red dots) and $\alpha-$ (black dots) of resonant electrons making maximal positive and main negative contributions to γ, respectively.

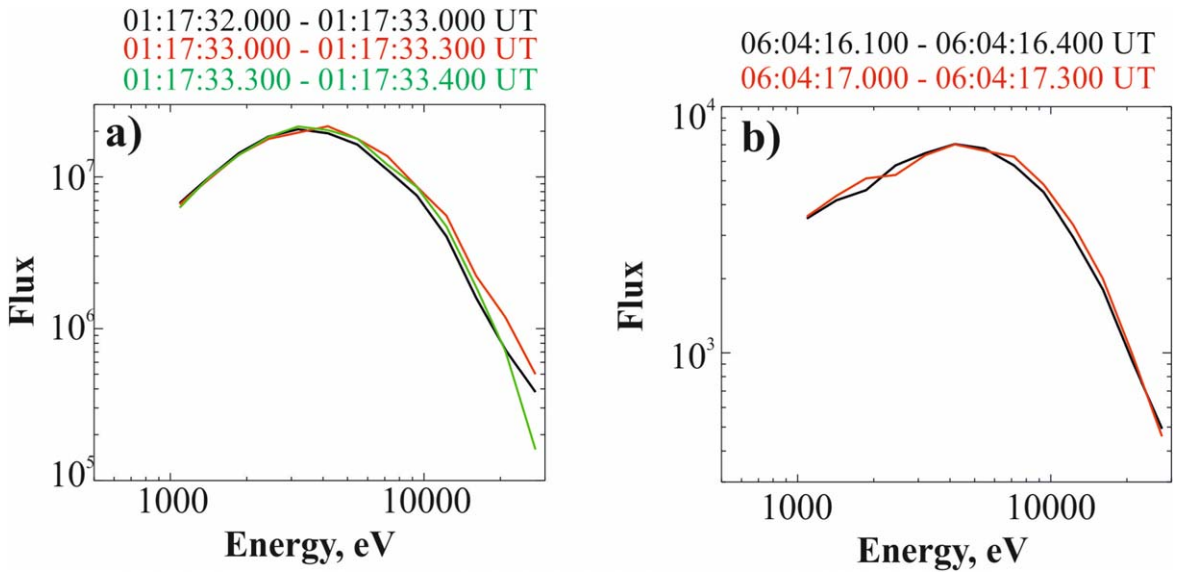

Figure 4. (a): Energy spectra of electron perpendicular flux measured on 2019 September 9 by MMS-1 at the moments specified at the top of this panel. (b): Energy spectra of electron perpendicular flux measured on 2017 July 17 by MMS-1 at the moments specified at the top of this panel.

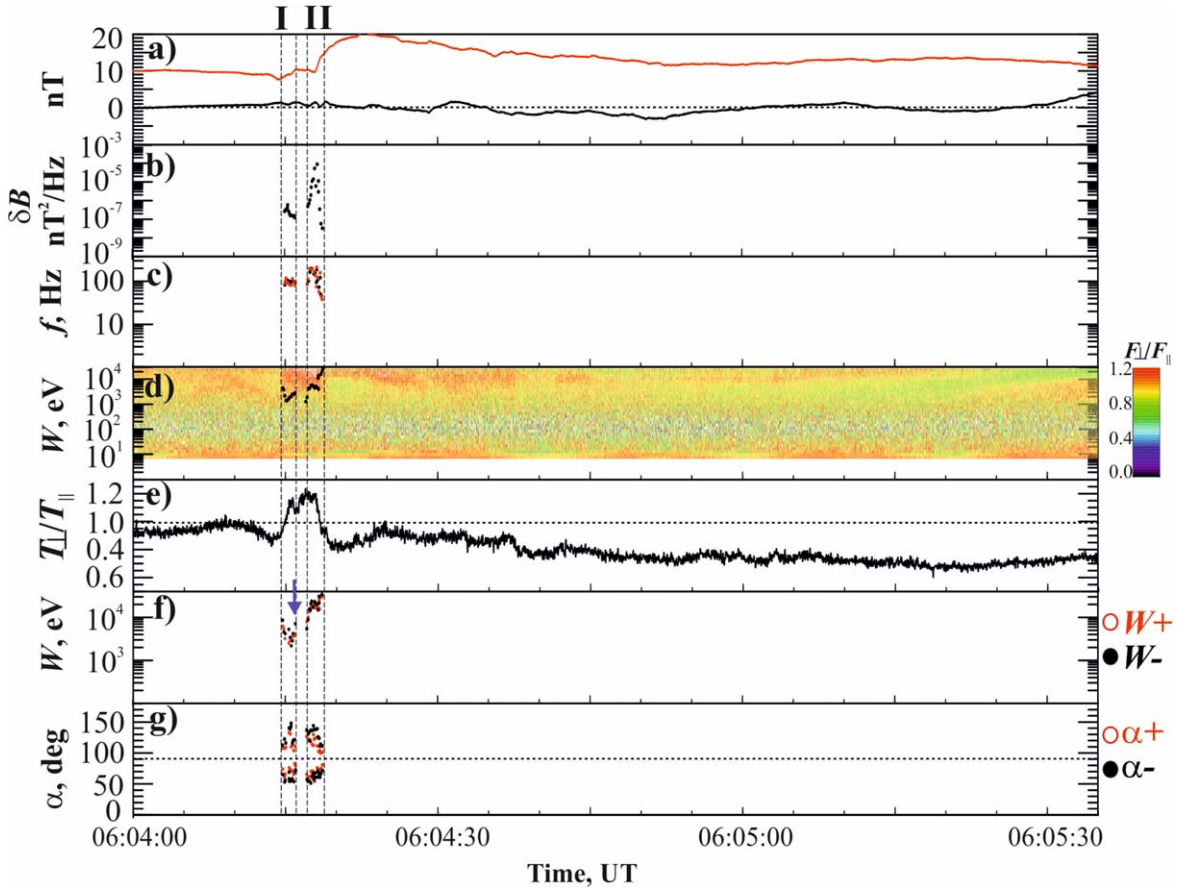

Figure 5. MMS-1 observations on 2017 July 17. The format of the figure is the same as that of Figure 3.

energy from the wave. In other words, the lower-energy population of resonant electrons transferred a part of its energy to the higher-energy electrons through the interactions with the whistler waves.

This effect is also observed in the dynamics of perpendicular fluxes of lower-energy and higher-energy electrons. Figure 4(a) shows the energy spectra of perpendicular electron fluxes measured during burst II and averaged over three time intervals specified at the top of the figure. At 01:17:33.000–01:17:33.300 UT, the flux of perpendicular electrons with energies ∼1–3 keV decreased, while in the higher-energy range (⩾4 keV) the flux increased simultaneously (see the red spectrum in Figure 4(a)). At this time $W-$ was larger than 4 keV and $W+$ was ∼1–3 keV (marked by the blue arrow in Figure 3(f)). Thus, electrons with $W_{\rm res} > 4$ keV absorbed some amount of energy from the wave, which may increase their perpendicular flux. Conversely, electrons with $W_{\rm res} \sim$ 1–3 keV transferred a part of their energy to the wave, which may cause the observed flux decrease in this energy range. Later during this burst, $W-$ decreased to ∼2 keV, and its value approached the value of $W+$. At this time, the flux of perpendicular electrons decreased in the high-energy range (see the green spectrum measured at 01:17:33.300–01:17:33.400 UT in Figure 4(a)).

Figure 5 presents the characteristics of resonant electrons interacting with the whistler bursts during the earthward bulk flow observed on July 17 at 06:04:00–06:05:35 UT. The format of the figure is similar to that of Figure 3. As in the previous event, the whistler waves are associated with the increase in energy-dependent perpendicular anisotropy of electron flux in the suprathermal energy range (>1 keV), and the parallel energies of resonant electrons $W_{||\_\rm res}$ are inside the energy range of the perpendicular flux anisotropy (see Figure 5(d)).

The total energies of resonant electrons $W_{\rm res}$ varied in a wide energy range, from ∼2 keV up to the high-energy threshold of the FPI instrument. The resonant electrons making the main positive contribution to γ have pitch angles $\alpha+ \sim 50°$–$80°$ and 100°–130° for the waves with $\boldsymbol{k}\cdot\boldsymbol{B} < 0$ and $\boldsymbol{k}\cdot\boldsymbol{B} > 0$, respectively. Similarly to the previous event, at each moment during the bursts the resonant electrons making the major negative contribution to γ are a little bit more field-aligned than electrons making the maximal positive contribution to γ, and they have $\alpha-$ in the ranges ∼50°–70° and 110°–150° for the waves with $\boldsymbol{k}\cdot\boldsymbol{B} < 0$ and $\boldsymbol{k}\cdot\boldsymbol{B} > 0$, respectively.

At some moments during the bursts, the energy of resonant electrons making the main negative contribution to γ ($W-$) was larger than the energy of resonant electrons making the main positive contribution to γ ($W+$) (see Figure 5(f)). At these moments the lower-energy resonant electrons transferred a part of their energy to the higher-energy electrons through wave–particle interactions. Figure 4(b) shows the energy spectra of perpendicular electron fluxes measured at the end of burst I and averaged over two time intervals specified at the top of the figure. At 06:04:17.000–06:04:17.300 UT, the flux of perpendicular electrons with energies ∼2–3 keV decreased (see the red spectrum in Figure 4(b)). Simultaneously, in the higher-energy range (⩾6 keV), the flux increased. At this time $W-$ was ∼6 keV and $W+$ was ∼3 keV (see the blue arrow in Figure 5(f)). Thus, as in the previous event, electrons with $W_{\rm res} \geqslant 6$ keV can absorb some energy from the wave and

increase their perpendicular flux, while electrons with lower energies can transfer a part of their energy to the wave and decrease their flux.

Summarizing the results of case studies, we suggest that the quasi-parallel narrowband whistler waves are often associated with the energy-dependent perpendicular anisotropy of electron fluxes observed in the suprathermal energy range. This corresponds to the increase in perpendicular temperature anisotropy only in those cases where the energy range of the resonant electrons is within the energy range measured by the FPI instrument. Almost simultaneously with the whistler bursts, the strong positive variations of perpendicular gradient of the magnetic field are observed at electron scales. The increase in this gradient could be responsible for the formation of perpendicular anisotropy of electron velocity distribution by betatron mechanism, which in turn can cause the whistler wave generation through excitation of electron cyclotron instability. In the next section we verify these suggestions statistically, and compare the results obtained for the tailward and earthward bulk flow intervals.

3. Statistical Studies

For the statistical studies, we use MMS observations of whistler bursts during 35 intervals of the tailward bulk flows and during 35 intervals of the earthward bulk flows (see a list of the intervals in the Appendix). The observations were made in the PS at $-25\ R_E \leqslant X \leqslant -17\ R_E$ and $|Y| \leqslant 11\ R_E$. To identify a quasi-parallel narrowband whistler wave, we use the method described by Grigorenko et al. (2020). During the intervals of earthward bulk flows, 3331 whistler wave moments were found, and during the tailward bulk flows we identified 6720 whistler wave moments. As the wave moment we term each moment of narrowband quasi-parallel whistler wave observation during each whistler burst. In this study we do not consider the oblique whistler waves, i.e., the waves with the wave normal angle $>40°$.

Figure 6 shows the characteristics of the narrowband whistler waves observed during the earthward and tailward bulk flows from our database. In both types of events, the majority of waves have the frequencies $\leqslant 0.6 f_{ce}$ (see Figure 6(a) and (d), respectively) and the wavelengths $\lambda \sim (1\text{–}1000)\rho_e$ (ρ_e is the gyroradius of thermal electrons) (see Figure 6(b) and (e), respectively). The values of average probabilities and their standard deviations (σ) are indicated in the corresponding panels of the figure. Figure 6(c) and (f) show the scatterplots of λ versus $|B_X|$ for the earthward and tailward bulk flow intervals, respectively. The whistler waves with various wavelengths (from $\sim 1\rho_e$ up to $\sim 1000\ \rho_e$) are observed at various distances from the neutral plane. The average values of λ and its standard deviations are indicated in the corresponding panels.

To reveal statistically where within the bulk flow the quasi-parallel narrowband whistler waves are more frequently observed, we apply a superposed epoch analysis to the intervals of the earthward and tailward bulk flows from our database. The epoch analysis was applied to the X-component of ion bulk velocity and B_Z field. For each event the V_X and B_Z were normalized to the corresponding maximum values observed in each event: $V_X^*(t) = V_X(t)/|V_{X\_\max}|$, $B_Z^*(t) = B_Z(t)/|B_{Z\_\max}|$. As the epoch time ($t_0 = 0$) we use the time when V_X started to increase (for the earthward flow intervals) or decrease to negative values (for the tailward flow intervals) from the background level.

Figure 7(a), (b), (d), and (e) present the epoch profiles of the aforementioned parameters for the intervals of the earthward and tailward bulk flows, respectively. The epoch profile of B_Z^*(t) during the earthward bulk flows exhibits a positive increase corresponding to the DF or DFB associated with the flows. For the tailward bulk flow intervals the B_Z^*(t) experiences multiple bipolar variations, which are observed during the entire flow interval.

Figure 7(c) and (f) show the distributions of the whistler wave occurrence frequency during the earthward and tailward epoch time intervals, respectively. The occurrence frequency was calculated as the ratio of the duration of whistler wave observation during each 5 s bin within the epoch time interval to the total number of MMS data samples within a given bin. During the earthward bulk flows the whistler waves are mainly observed in the DFBs associated with the earthward bulk flows. Near the trailing edge of the earthward bulk flows and outside the DFB, the occurrence frequency of whistler waves significantly decreases. Conversely, during the intervals of tailward bulk flows, the whistler waves are observed almost with the same probability during the entire flow interval, similarly to the B_Z bipolar variations. We suggest that during the tailward bulk flows the whistler waves appear in the vicinity of flux ropes/magnetic islands transported by the bulk flows. Thus, the difference in the distribution of whistler wave occurrence frequency during the earthward and tailward bulk flows can be caused by the difference in the magnetic structure of the flows.

Figure 8(a) and (e) show the distribution of whistler wave occurrence frequency versus the distance from the neutral plane during the earthward and tailward bulk flows, respectively. We use the value of $|B_X|$ as a proxy for the distance from the neutral plane. The occurrence frequency was calculated as the ratio of the total whistler wave duration during the time intervals when the MMS spacecraft were located within a given $|B_X|$ bin to the total time of the MMS location within this bin regardless of whether the whistler waves were observed.

The gray shaded distributions display the occurrence frequency of whistler waves that were generated either in a remote source(s) or locally. To study the distribution of the sources of whistler waves as a function of $|B_X|$, we calculated the occurrence frequency only for those waves, for which the condition (2) was fulfilled. These distributions are shaded in red in Figure 8(a) and (e). During the earthward bulk flows, the occurrence frequency of the waves generated locally maximizes closer to the neutral plane, while during the tailward flow intervals, the sources of quasi-parallel whistler waves are distributed over the PS.

Figure 8(b) presents the distribution of whistler wave observation probability versus the time lag, Δt, between each whistler wave moment and the nearest positive variation of $(\nabla B)_\perp$ having an amplitude larger than $0.7 * [(\nabla B)_\perp]_{\max}$. Here, $[(\nabla B)_\perp]_{\max}$ is the absolute maximal value of positive $(\nabla B)_\perp$ observed in a given interval of the earthward high-velocity bulk flow from our database. Figure 8(f) displays the same distribution obtained for the tailward bulk flow intervals. To construct the distributions, we used only those wave moments at which the condition (2) was fulfilled, i.e., the moments when the wave source was most likely located near the spacecraft. During both the earthward and tailward bulk flow intervals the distributions maximize near the $\Delta t = 0$. This means that in the majority of cases the generation of quasi-parallel narrowband

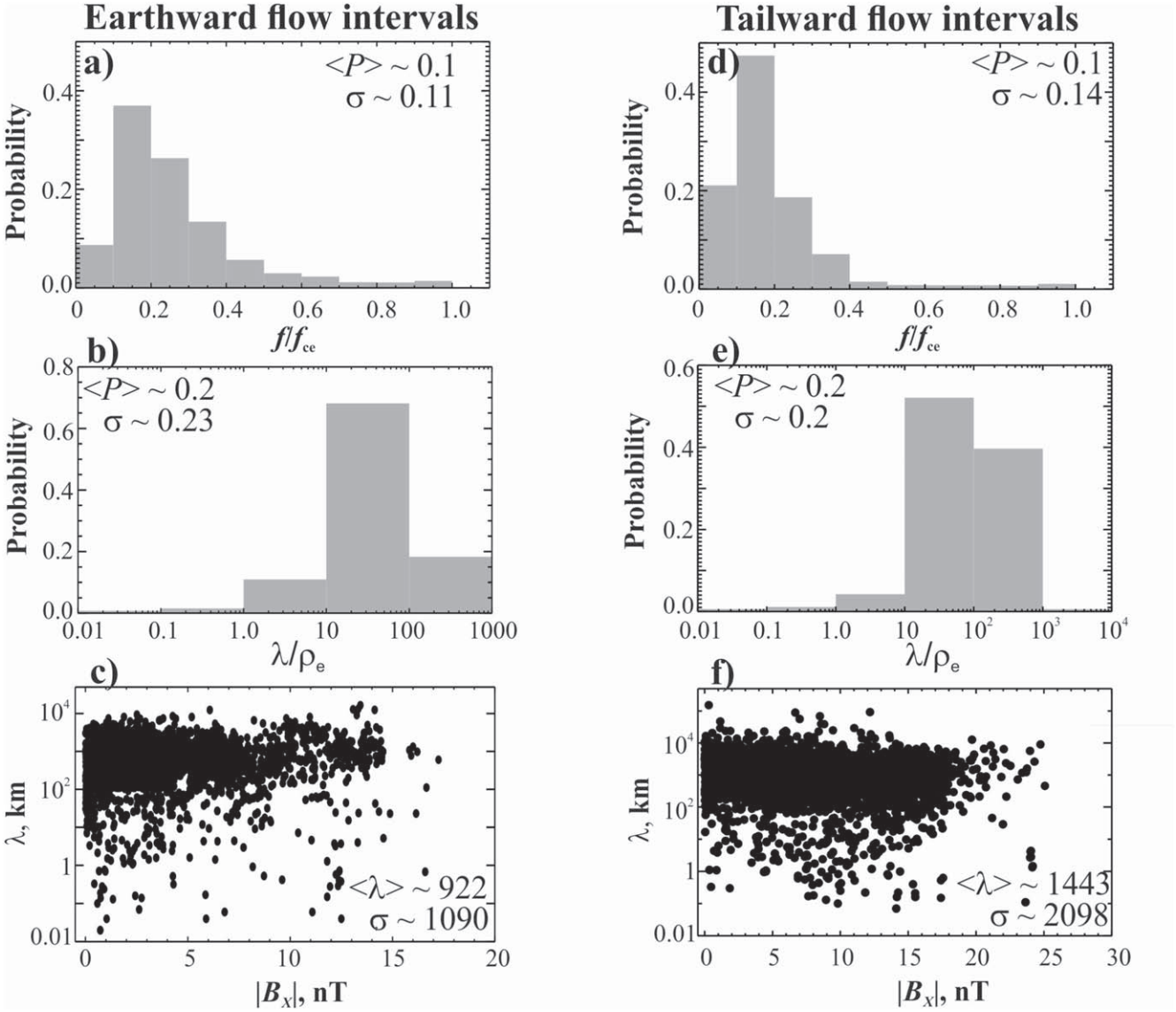

Figure 6. The distributions of probability to observe the following characteristics of quasi-parallel narrowband whistler waves: the observed wave frequency normalized to the local electron gyrofrequency, f_w/f_{ce}, for the earthward (a) and tailward (d) bulk flows; the whistler wave wavelength normalized to the local gyroradius of thermal electrons, λ/ρ_e, for the earthward (b) and tailward (e) bulk flows. The scatterplots of λ vs. $|B_X|$ for the earthward (c) and tailward (f) bulk flows.

whistler waves was associated with the strong positive variations in perpendicular gradient of the magnetic field observed at electron kinetic scales.

Figure 8(c) and (g) show the distribution of probability to observe the whistler waves versus the local value of electron $\frac{T_\perp}{T_\parallel}$. During the earthward bulk flows the majority of whistler waves are associated with the perpendicular temperature anisotropy of electrons ($\frac{T_\perp}{T_\parallel} > 1$). Conversely, during the tailward bulk flows a significant fraction of whistler waves was observed at the moments when $\frac{T_\perp}{T_\parallel} < 1$. In the tailward flow event discussed in the case study section, burst III (see Figure 1) was associated with the parallel electron temperature anisotropy. For this burst the magnitudes of parallel energies of resonant electrons $W_{||\_res}$ were close to the high-energy threshold of the FPI instrument. In such a case, the temperature anisotropy of electron population measured in the FPI energy range does not show the real anisotropy of a high-energy population of resonant electrons contributing to γ.

To check this statistically, we make the scatterplots of $W_{||\_res}$ versus the local values of $\frac{T_\perp}{T_\parallel}$ for the earthward (Figure 8(d)) and tailward (Figure 8(h)) bulk flow intervals. For these scatterplots we use only those wave moments at which the condition (2) was fulfilled. During the earthward bulk flows, in the majority of wave moments when electron temperature anisotropy was parallel ($\frac{T_\perp}{T_\parallel} < 1$), the $W_{||\_res}$ exceeded 10 keV, and the total energy of resonant electrons was even higher and approached the FPI high-energy threshold. At the moments when $W_{||\_res}$ was lower (<10 keV), i.e., the entire population of resonant electrons was well observed by the FPI instrument, the $\frac{T_\perp}{T_\parallel} > 1$. Thus, we suggest that during the earthward bulk flow intervals the generation of whistler waves could be mostly due to the perpendicular temperature anisotropy of electron distribution.

During the tailward bulk flow intervals the tendency of $\frac{T_\perp}{T_\parallel}$ increase with the decrease in $W_{||\_res}$ is not so clearly observed. Nevertheless, at the majority of wave moments when $\frac{T_\perp}{T_\parallel} < 1$

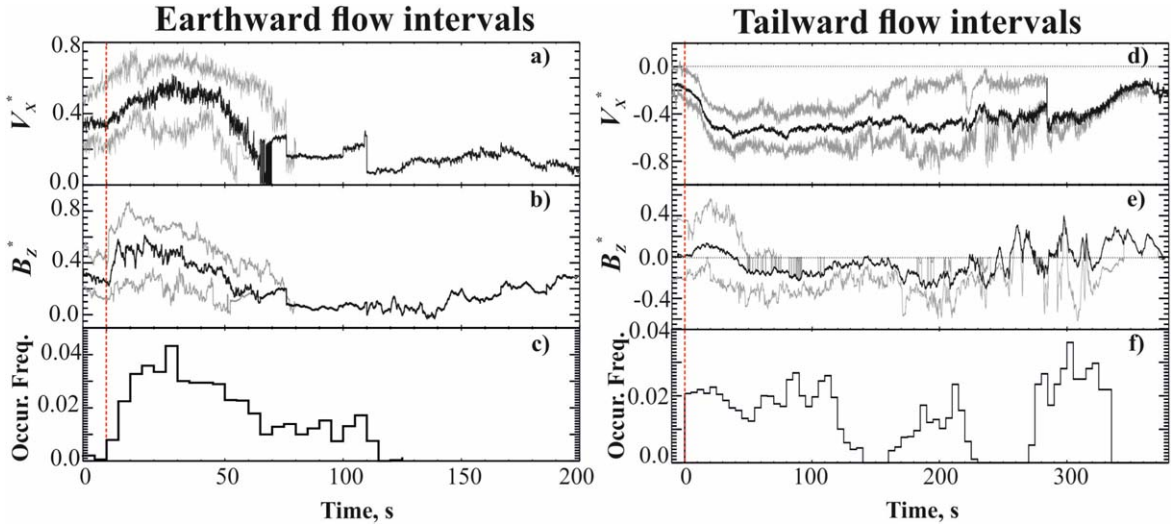

Figure 7. The epoch profiles of the following parameters: $V_X^*(t)$ and $B_Z^*(t)$ obtained for the intervals of the earthward (a), (b) and tailward (d), (e) bulk flows, respectively. The distributions of whistler wave occurrence frequency during the earthward (c) and tailward (f) epoch time intervals. The vertical red dashed line marks the epoch time $t = 0$. The gray lines show low and upper quartiles.

the resonant electrons have the $W_{||\_res}$ more than a few keV. For such moments we suggest that electron cyclotron instability responsible for the whistler wave generation could be excited due to the perpendicular anisotropy of the high-energy electron population, which was not well observed by the FPI. At those wave moments when $\frac{T_\perp}{T_\parallel} < 1$ and the resonant energies of electrons were inside the FPI energy range, some other mechanism could be responsible for the whistler wave generation. Using the method described in the previous section, we determined the total energies $W_{res} = W_{||\_res}/\cos^2\alpha$ and pitch angles, α_{res}, of the resonant electrons making the maximum contribution to the growth rate, γ, for all wave moments at which the condition (2) was fulfilled. Figure 9(a) and (d) show the statistical distributions of W_{res} for the earthward and tailward bulk flow intervals, respectively. During the earthward bulk flow intervals, the distribution of W_{res} maximizes at ~1 keV, and in the majority of the wave moments $W_{res} < 10$ keV. During the tailward bulk flow intervals, the maximum of W_{res} distribution is also located at ~1 keV. However, during these intervals the distribution is more extended in the high-energy range, and at many wave moments, the total energy of resonant electrons is larger than 10 keV.

Figure 9(b) and (e) present the statistical distributions of α_{res} of resonant electrons making maximum contribution to γ of the waves propagating parallel ($\boldsymbol{k}\cdot\boldsymbol{B} > 0$) and antiparallel ($\boldsymbol{k}\cdot\boldsymbol{B} < 0$) to the ambient magnetic field. In the majority of the earthward flow events, electrons with $\alpha_{res} \sim 100°$–$140°$ make maximum contribution to the growth rate of the waves with $\boldsymbol{k}\cdot\boldsymbol{B} > 0$, while electrons with $\alpha_{res} \sim 40°$–$80°$ contribute to the growth rate of the whistler waves with $\boldsymbol{k}\cdot\boldsymbol{B} < 0$ (see Figure 8(b)). During the tailward bulk flow intervals, electrons with $\alpha_{res} \sim 130°$–$160°$ make maximum contribution to the growth rate of the waves with $\boldsymbol{k}\cdot\boldsymbol{B} > 0$, while electrons with $\alpha_{res} \sim 20°$–$60°$ contribute to the growth rate of the whistler waves with $\boldsymbol{k}\cdot\boldsymbol{B} < 0$.

Thus, during the earthward flow intervals, suprathermal electrons with pitch angles rather close to ~60° and ~120° and moving in the opposite direction of the waves efficiently interact with the quasi-parallel whistler waves and transfer to them a part of their kinetic energy. During the tailward flow intervals, electrons with $\alpha_{res} \sim 40°$ and ~145° interact efficiently with the whistler waves propagating antiparallel and parallel to the ambient magnetic field, respectively. Electrons with α_{res} close to 0° or 180° do not contribute to the growth rate of quasi-parallel whistler waves. We would like to stress that, when we speak about electrons making the main contribution to the growth rate, we always mean the frequency that corresponds to maximum growth rate, that is, the frequency of the most unstable wave (f_γ).

In the previous section we discussed the energy exchange between populations of resonant electrons through their interactions with the whistler waves. Some fraction of resonant electrons, which make a positive contribution to γ, transfers a part of their energy to the wave and decreases their perpendicular anisotropy. Simultaneously, the other population of resonant electrons makes a negative contribution to γ and thus absorbs the energy from the wave and increases their perpendicular anisotropy. Interestingly, at some moments electrons with lower energies can transfer a part of their energy to the higher-energy population through the interactions with the whistler waves. This process could be responsible for the formation of energy-dependent perpendicular anisotropy of electron flux observed in the high-energy range, and for the formation of the power-law tails in the high-energy part of the electron spectrum.

To study statistically how often and at which distances from the neutral plane such energy exchange occurs, we determined the total energies of resonant electrons making the maximal positive ($W+$) and the main negative ($W-$) contributions to γ at each wave moment during the earthward and tailward bulk flow intervals from our database. Figure 9(c) and (f) present the scatterplots of the ratio $W+/W-$ versus $|B_X|$. It is seen that there are a lot of wave moments when $W+/W- < 1$; i.e., the lower-energy resonant electrons transfer their energy to the higher-energy resonant electrons via the interactions with the whistler waves. During both earthward and tailward bulk flow intervals, such processes are observed mainly in the vicinity of the neutral plane and at the Central PS (in the region with $|B_X| < 10$ nT). Thus, in this region one may expect the formation of energy-dependent perpendicular anisotropy and power-law tails in the higher-energy range of electron distribution during the intervals of whistler bursts. Moreover, because the lower-energy part of electron distribution is more abundant than the higher-energy part, such energy transfer

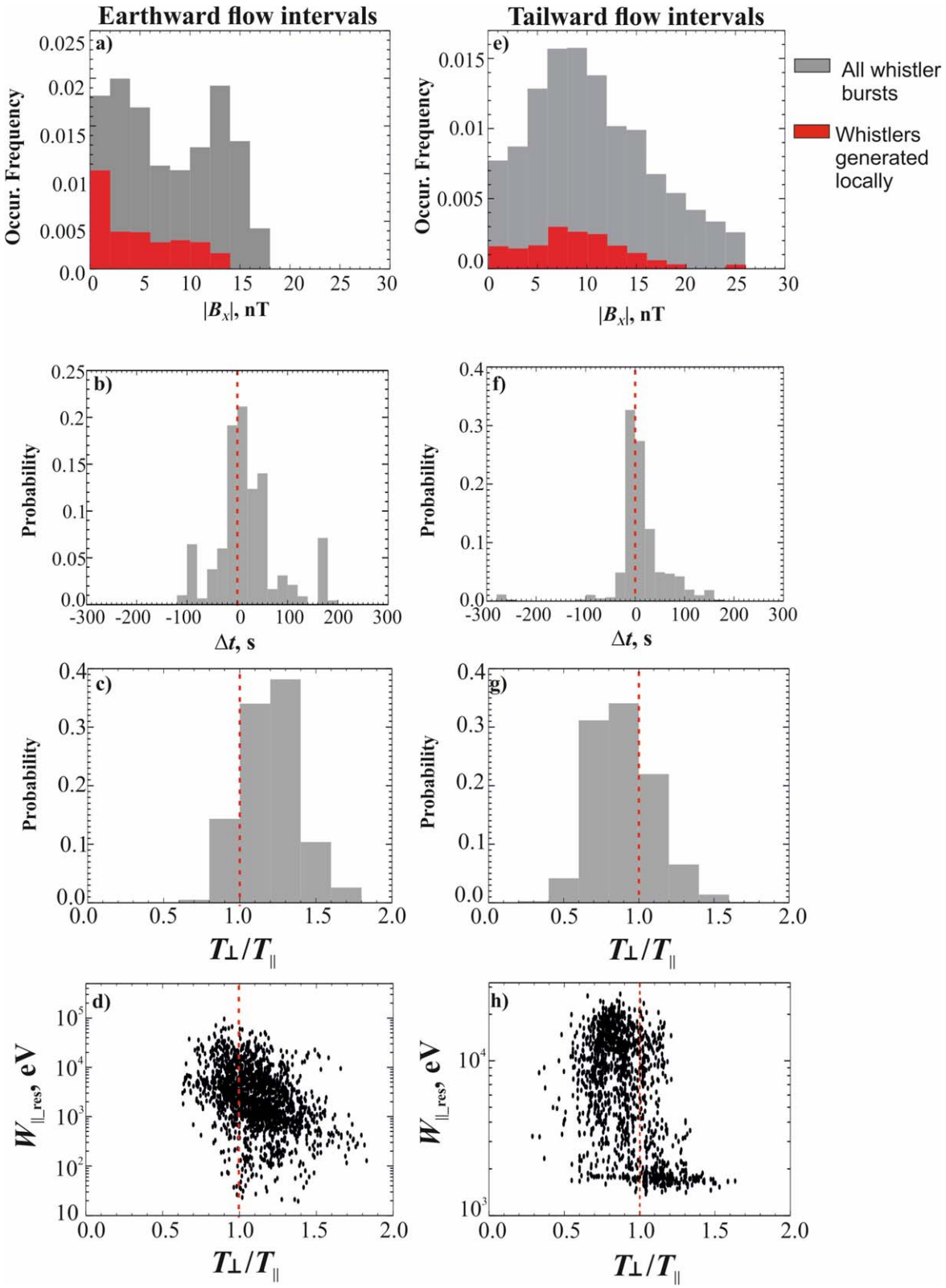

Figure 8. The distribution of whistler wave occurrence frequency vs. $|B_X|$ during the earthward (a) and tailward (e) bulk flow intervals. The gray distribution is constructed for all whistler wave moments from our database. The red distribution is constructed for the waves that are most likely generated locally. The distribution of probability to observe the whistler waves vs. the time lag, Δt, between the wave observation and the moment of the strong positive $(\nabla B)_\perp$ increase (see explanation in the text) for the earthward (b) and tailward (f) bulk flow intervals. The distribution of probability to observe the whistler waves vs. electron $\frac{T_\perp}{T_\parallel}$ obtained for the intervals of earthward (c) and tailward (g) bulk flows. The scatterplots of $W_{\parallel\_res}$ vs. $\frac{T_\perp}{T_\parallel}$ obtained for the intervals of earthward (d) and tailward (h) bulk flows.

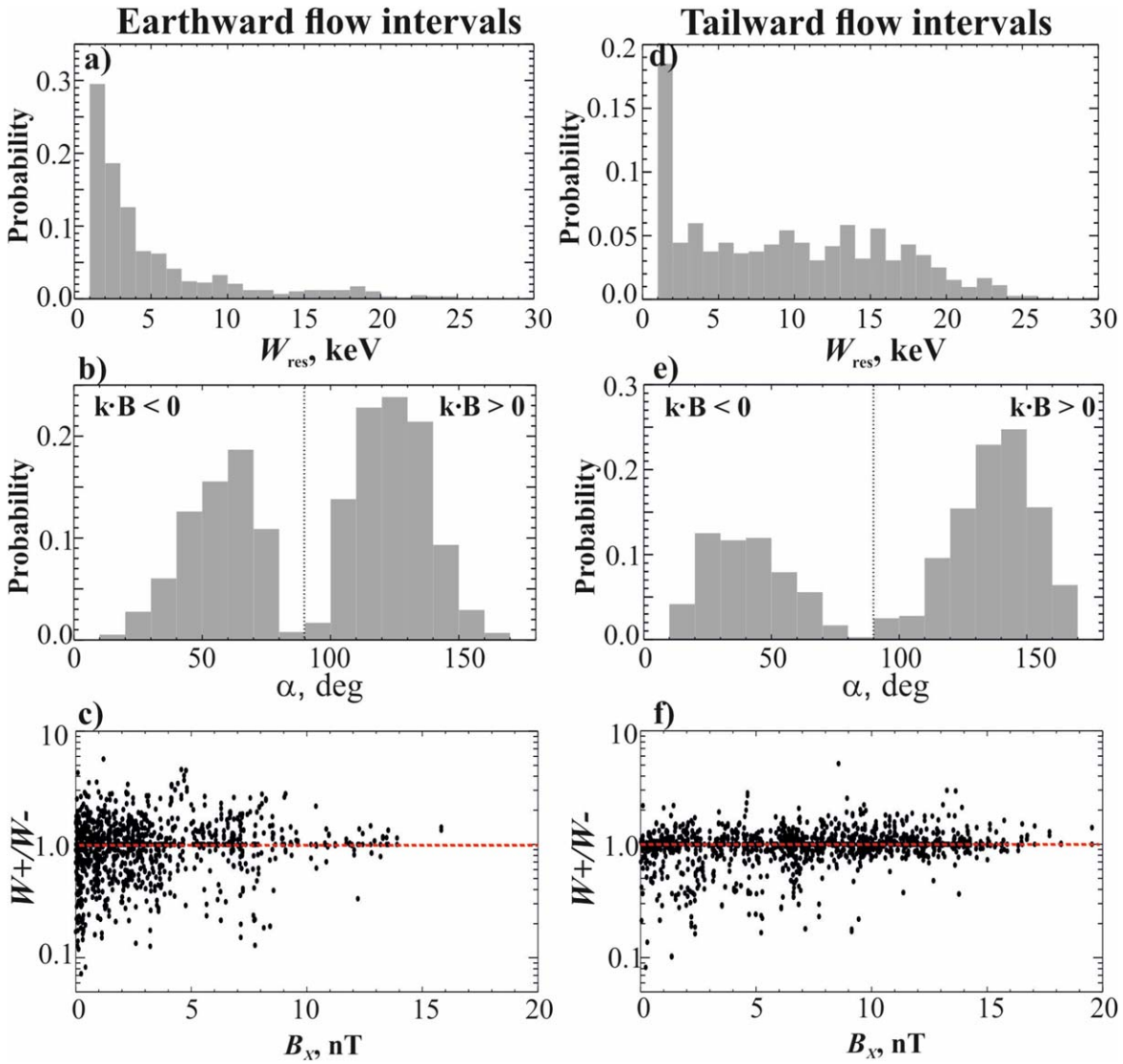

Figure 9. The distributions of probability to observe: the given values of the total energy of resonant electrons, W_{res}, during the intervals of the earthward (a) and tailward (d) bulk flows; the given values of pitch angles α_{res} of resonant electrons making maximum contribution to γ of the waves propagating parallel ($\boldsymbol{k} \cdot \boldsymbol{B} > 0$) and antiparallel ($\boldsymbol{k} \cdot \boldsymbol{B} < 0$) to the ambient magnetic field for the intervals of the earthward (b) and tailward (e) bulk flows. The scatterplots of $W+/W-$ vs. $|B_X|$ for the intervals of earthward (c) and tailward (f) bulk flows.

may cause the generation or amplification of the whistler waves near the neutral plane and in the Central PS. This is confirmed by the statistical distribution of whistler wave occurrence frequency presented in Figure 8(a) and (e) as well as by previous studies (e.g., Le Contel et al. 2009). The probability of such energy exchange between the lower-energy and higher-energy electrons decreases with the distance from the neutral plane, and in the outer PS (in the region with $|B_X| > 10$ nT), such a process occurs rarely. In this PS region, in the majority of wave moments electrons with higher energies transfer a part of their kinetic energy to the whistler waves, while the electrons with lower energy absorb the energy from the wave. Because the lower-energy electron population is more abundant than the higher-energy one, such processes may cause the wave damping in the outer PS region.

4. Discussion

In this paper we present a comparative analysis of the characteristics of quasi-parallel whistler waves and resonant electrons interacting with these waves during the intervals of the earthward and tailward bulk flows. Our studies focus on the bulk flows observed by MMS in the PS at $-25 \leqslant X \leqslant -17\ R_E$, i.e., in the regions located on both sides of the X-line outside the diffusion region. The magnetic structure of the earthward and tailward bulk flows is quite different, as are the conditions of their propagation in the magnetotail. Therefore, it is worth investigating whether these differences influence the characteristics of whistler waves and the properties of resonant electrons. Below we summarize our findings.

1. During both earthward and tailward bulk flows, the narrowband quasi-parallel whistler wave is observed as a bulge in frequency spectra of the PSD of the magnetic field fluctuations. The majority of waves have the frequencies $f \leqslant 0.6 f_{ce}$ (see Figure 6(a) and (d)). The duration of whistler bursts ~a few seconds or less. The majority of whistler waves have the wavelengths ~(1–1000)ρ_e (see Figures 6(b) and (e)).
2. During the earthward bulk flows from our database, the whistler waves were observed mainly at the DFs and in

the DFB behind the DFs. The occurrence frequency of whistler waves decreased near the trailing edge of the earthward bulk flows outside the DFB (see Figure 7(a)–(c)). Conversely, during the tailward bulk flows the whistler waves were observed during the entire flow interval (see Figures 7(d)–(f)).

3. During the intervals of the earthward bulk flows, the occurrence frequency of whistler waves that are likely generated locally is maximal near the neutral plane (see the red histogram in Figure 8(a)). During the intervals of the tailward bulk flows, the sources of whistler waves are distributed over the PS (see Figure 8(e)).
4. During both the earthward and tailward bulk flow intervals, the generation of quasi-parallel narrowband whistler waves was often associated with the strong positive variations in the perpendicular gradient of the magnetic field observed at electron kinetic scales (see Figure 8(b) and (f)).
5. During the earthward bulk flows, the majority of whistler waves are associated with the perpendicular temperature anisotropy of electrons (see Figure 8(c)). However, during the tailward bulk flow intervals, a lot of whistler waves are observed during the intervals of parallel electron temperature anisotropy (see Figure 8(g)).
6. During the earthward bulk flow intervals, electrons with pitch angles $\alpha_{res} \sim 100°$–$140°$ and $\alpha_{res} \sim 40°$–$80°$ made maximum contribution to the growth rate, γ, of whistler waves propagating parallel ($\boldsymbol{k}\cdot\boldsymbol{B} > 0$) and antiparallel ($\boldsymbol{k}\cdot\boldsymbol{B} < 0$) to the ambient magnetic field, respectively (see Figure 9(b)). During the intervals of the tailward bulk flows, electrons with $\alpha_{res} \sim 130°$–$160°$ and $\alpha_{res} \sim 20°$–$60°$ contributed to γ of whistler waves with $\boldsymbol{k}\cdot\boldsymbol{B} > 0$ and $\boldsymbol{k}\cdot\boldsymbol{B} < 0$, respectively (see Figure 9(e)).
7. In the majority of earthward bulk flow intervals, the total energy of resonant electrons making the maximal positive contribution to γ was $W_{res} \sim 1$–10 keV (see Figure 9(a)). For the tailward bulk flow intervals, W_{res} ranged between $\sim$1 and $\sim$25 keV (see Figure 9(d)).
8. During both earthward and tailward bulk flow intervals, the lower-energy resonant electrons may transfer a part of their energy to higher-energy resonant electrons through the interactions with quasi-parallel whistler waves. Such processes are mainly observed in the vicinity of the neutral plane and in the Central PS (in the region with $|B_X| < 10$ nT, see Figure 9(c) and (f)).

Previous studies reported that electron cyclotron instability could be responsible for the generation of quasi-parallel whistler waves due to the presence of perpendicular temperature anisotropy of electrons (e.g., Sagdeev & Shafranov 1961; Kennel 1966). Specifically, this mechanism was confirmed for DFs and DFB regions in the magnetotail PS, where the betatron acceleration of background electrons forms the perpendicular anisotropy of electron distribution (e.g., Khotyaintsev et al. 2011; Huang et al. 2012; Grigorenko et al. 2020). Indeed, the statistical studies presented in this paper showed that during the intervals of earthward bulk flows, the quasi-parallel narrowband whistler waves are observed at and behind the DFs in the region of DFBs where $\frac{T_\perp}{T_\parallel} > 1$.

During the intervals of the tailward bulk flows, i.e., tailward from the X-line, the quasi-parallel whistler waves have the characteristics (the frequency range, wavelengths, and ellipticity) similar to those observed during the earthward bulk flows. But at many wave moments, the electron temperature anisotropy was parallel ($\frac{T_\perp}{T_\parallel} < 1$).

The temperature anisotropy is an integral parameter calculated in a certain energy range determined by the instrument capabilities. In those cases, when the energy of resonant electrons is near or exceeds the high-energy threshold of the instrument, the observed temperature anisotropy does not show the real anisotropy of the electron population responsible for whistler wave generation (e.g., Malykhin et al. 2021). Indeed, at many wave moments when $\frac{T_\perp}{T_\parallel} < 1$ was observed, the parallel energy of resonant electrons was larger than 10 keV, so that their total energy approached or exceeded the high-energy threshold of the FPI instrument (see Figure 8(d) and (h)).

Another possible mechanism of quasi-parallel whistler wave generation can be the parametric coupling of lower hybrid oblique resonance and plasma density irregularities or extremely low-frequency waves (Mishin et al. 2019; Main & Sotnikov 2020). The oblique lower hybrid waves are often observed near DFs and ADFs, and their scattering due to the interactions with density irregularities can produce the whistler waves with similar frequencies and small wave normal angles. We are going to study a role of this mechanism in the generation of the quasi-parallel whistler waves near DFs and ADFs in our future work.

Using MMS observations in burst mode, we calculate the growth rate of quasi-parallel whistler waves from 3D electron velocity distribution functions averaged over 120 ms within each burst of whistler waves from our database. Then, at each moment we determine the total energies and pitch angles of the resonant electrons making maximum positive ($W+$, $\alpha+$) and the strongest negative ($W-$, $\alpha-$) contributions to the growth rate. We have found that both during the earthward and tailward bulk flow intervals, the suprathermal electrons ($\geqslant$1 keV) with large pitch angles efficiently interact with the whistler waves and participate in the processes of energy exchange with the waves (see Figure 9(a), (b), (d), and (e)).

The energy exchange between particles and waves affects the particle anisotropy. Specifically, those electrons that make positive contributions to γ and thus transfer a part of their energy to the wave decrease their perpendicular anisotropy. Conversely, electrons making negative contributions to γ obtain energy from the wave and increase their anisotropy. Because both $W+$ and $W-$ are in the suprathermal energy range for all whistler waves from our database, one may expect that the significant modulation of perpendicular anisotropy of electron flux occurs in the suprathermal energy range. This is in agreement with the previous results obtained by Zhao et al. (2019), who indicated the energy $\sim$1.7 keV ("anchor point"), which breaks the electron distribution function into lower-energy Maxwellian and higher-energy power-law parts. Also Liu & Fu (2019), using the large volume of Cluster observations, statistically showed that the formation of the "anchor point" correlates with the strong wave activity. In this paper we show that during both the earthward and tailward bulk flows, the energy-dependent perpendicular anisotropy of electron flux is enhanced in the suprathermal energy range during the whistler bursts. This feature is more clearly observed when the energy of resonant electrons is inside the energy range of the FPI instrument.

To check if the observed whistler wave is generated close to MMS spacecraft, we have compared the observed frequency of the whistler waves (f_w) with the frequency corresponding to the

maximum growth rate (f_γ) calculated from the local 3D electron velocity distribution at each moment within the burst. We suggest that if $|f_w - f_\gamma|/f_w$ value calculated for every 120 ms is equal or less than 0.2, then the anisotropy of local electron velocity distribution function could be responsible for the whistler wave generation; i.e., the wave source is located near MMS spacecraft. We found that during the earthward bulk flows, this condition is fulfilled mainly in the vicinity of the neutral plane (see Figure 8(a)). During the intervals of the tailward bulk flows, the sources of whistler wave are more widely distributed over the PS (see Figure 8(e)). This difference can be due to the different magnetic structures of the earthward and tailward bulk flows.

If the observed quasi-parallel narrowband whistler waves are generated due to electron cyclotron instability, then the question is which mechanism is responsible for the formation of the perpendicular anisotropy of electron velocity distribution function triggering this instability? During the intervals of the earthward bulk flows, the betatron acceleration of electrons in DFs/DFBs forms the perpendicular anisotropy of electron distribution (e.g., Fu et al. 2011; Khotyaintsev et al. 2011). On the tailward side of the X-line, the compression due to the flow braking in the region of strong magnetic field does not occur and the formation mechanism of perpendicular electron anisotropy is not so clear.

Generally, the betatron acceleration is caused by the transient enhancement of the magnetic field. Therefore, we checked the relation between the positive variation of the perpendicular gradient of the magnetic field and the whistler wave observations during both earthward and tailward bulk flow intervals. We found that in both groups of events, the majority of whistler waves are observed almost simultaneously with the strong positive variation of the perpendicular gradient of the magnetic field (with amplitudes $\geqslant 1 \times 10^{-5}$ nT m^{-1}) measured within the MMS tetrahedron. The appearance of such gradients enhances the perpendicular electron flux, especially in the higher-energy range, and forms the perpendicular anisotropy of electron velocity distribution in the suprathermal energy range, which could be responsible for the whistler wave generation. The observation of strong small-scale magnetic gradients in the vicinity of DFs and in DFBs has been reported before in many studies (e.g., Balikhin et al. 2014; Grigorenko et al. 2018; Liu et al. 2018; Nakamura et al. 2018). Here we found that during the tailward bulk flows, the small-scale perpendicular magnetic gradients are often observed near magnetic flux ropes almost simultaneously with the quasi-parallel narrowband whistler waves.

In collisionless plasma, wave–particle interactions are an important tool for energy exchange between different plasma populations as well as for particle energization. The excitation of whistler waves by unstable electron distribution is accompanied by energy exchange between electrons with different perpendicular velocities through the excited waves. In some cases this can lead to energy transfer from lower- to higher-energy particles (e.g., Shklyar 2011, 2017). In the case study presented by Grigorenko et al. (2020), it was shown that such a process indeed occurs at the DF. In this paper we statistically investigate the ratio of the energy of resonant electrons making the maximum positive contribution to γ ($W+$) to the energy of resonant electrons making the strongest negative contribution to γ ($W-$) calculated at each moment within each wave burst from our database (see Figure 9(c) and (f)). During both earthward and tailward bulk flow intervals, there are many moments when $W+/W- < 1$, especially near the neutral plane and in the Central PS (at $|B_X| < 10$ nT). Such a process contributes to the increase in electron perpendicular flux in the higher-energy range and to the formation of the power-law tails in electron energy spectrum in these regions.

5. Conclusions

Using MMS observations in burst mode we compared the characteristics of quasi-parallel narrowband whistler waves, their occurrence frequency, and peculiarities of interactions with resonant electrons during the intervals of earthward and tailward bulk flows in the Earth's magnetotail. We found that during both types of events, electrons with large pitch angles and energies >1 keV make maximum contributions to whistler wave growth rate. For the majority of wave moments when the energy of resonant electrons was inside the energy range of the FPI instrument, the perpendicular temperature anisotropy of electrons was observed. Thus, in many cases from our database, the generation of quasi-parallel narrowband whistler waves is likely related to the electron cyclotron instability excited by the perpendicular anisotropy of electron velocity distribution in the resonant energy range. The majority of the whistler waves were observed almost simultaneously with the transient enhancements of the perpendicular gradients of the magnetic field appearing at DFs and DFBs in the earthward bulk flows and in the vicinity of flux ropes in the tailward bulk flows. The betatron energization of electrons due to the transient appearance of such gradients may increase the perpendicular anisotropy of electron distribution responsible for the quasi-parallel whistler wave generation. Thus, despite the differences in the magnetic structure of the earthward and tailward bulk flows, the mechanisms of the quasi-parallel whistler wave generation could be the same there. Finally, we have shown that whistler waves play an important role in modulation of the electron energy spectrum and their anisotropy in the suprathermal energy range. The processes of energy transfer from lower-energy to higher-energy populations of resonant electrons through the interactions with the waves could be responsible for the formation of energy-dependent perpendicular anisotropy of electron flux and power-law tails in the high-energy part of the electron spectrum, especially near the magnetotail neutral plane and in the Central PS.

We thank the MMS Data Center (https://lasp.colorado.edu/mms/sdc/public/), from which the data used in this paper were obtained. The authors thank Professor D. Shklyar for his great help and valuable comments. The work of E.E.G., A.Y. M., and E.A.K. is partially supported by the Volkswagen Foundation (grant # 97742). E.A.K. is also supported by the German Research Foundation (DFG) under number KR 4375/2-1 within SPP "Dynamic Earth." The work of E.V.P. is supported by the Austrian Science Fund (FWF): I 3506-N27.

Appendix

In Table 1 we present time intervals of the earthward and tailward high-velocity bulk flows used in this study.

Table 1
List of the Earthward and Tailward High-velocity Bulk Flow Intervals

Earthward Bulk Flow Intervals, (UT)	Tailward Bulk Flow Intervals, (UT)
2017 Jun 5 13:36:10–13:37:15	2017 Jun 11 16:58:00–17:02:00
2017 Jun 17 14:41:40–14:45:00	2017 Jul 11 23:45:00–23:46:00
2017 Jun 19 03:57:10–03:58:00	2017 Jul 17 09:05:20–09:07:05
2017 Jun 19 03:58:40–03:59:20	2017 Jul 17 09:10:00–09:11:25
2017 Jun 19 04:01:20–04:02:30	2017 Jul 17 13:26:35–13:28:40
2017 Jun 19 04:02:45–04:04:35	2017 Jul 18 05:04:00–05:10:20
2017 Jun 20 16:03:35–16:04:45	2017 Jul 18 05:10:40–05:14:30
2017 Jun 20 16:05:10–16:06:30	2017 Jul 25 23:56:00–23:59:00
2017 Jun 22 11:01:00–11:03:50	2017 Jul 26 10:13:00–10:18:00
2017 Jun 25 04:24:42–04:26:35	2017 Aug 1 10:54:00–10:58:20
2017 Jun 30 23:18:00–23:25:40	2017 Aug 1 11:15:00–11:16:10
2017 Jul 3 22:45:30–22:47:30	2017 Aug 1 11:26:49–11:27:35
2017 Jul 8 21:14:00–21:16:00	2017 Aug 1 11:27:40–11:28:50
2017 Jul 9 10:46:00–10:46:23	2017 Aug 1 13:39:20–13:42:00
2017 Jul 9 10:46:54–10:48:20	2017 Aug 6 05:09:00–05:10:40
2017 Jul 9 10:49:30–10:50:40	2017 Aug 6 05:11:20–05:14:50
2017 Jul 9 17:37:30–17:37:48	2017 Aug 21 00:36:00–00:39:00
2017 Jul 9 17:36:18–17:38:22	2018 Aug 15 12:16:30–12:18:40
2017 Jul 9 17:38:23–17:39:11	2018 Aug 21 10:55:50–11:01:10
2017 Jul 17 06:04:10–06:05:25	2018 Aug 27 16:37:30–16:40:30
2017 Jul 17 07:52:43–07:53:22	2019 Aug 1 22:28:00–22:30:00
2017 Jul 17 14:51:00–14:53:10	2019 Aug 5 15:15:30–15:19:30
2017 Jul 20 11:43:10–11:46:50	2019 Aug 8 13:57:20–14:00:00
2017 Jul 24 12:49:00–12:50:50	2019 Aug 8 14:02:00–14:04:00
2017 Jul 25 22:09:40–22:10:50	2019 Aug 12 14:10:00–14:14:10
2017 Jul 26 11:31:35–11:33:54	2019 Aug 15 20:40:45–20:47:00
2017 Jul 29 08:22:10–08:24:00	2019 Aug 31 11:53:00–11:57:04
2017 Jul 29 15:58:40–15:59:55	2019 Sep 1 07:21:37–07:24:30
2017 Jul 31 20:58:00–21:00:35	2019 Sep 5 20:48:15–20:51:30
2017 Jul 31 21:36:40–21:39:00	2019 Sep 5 21:08:33–21:10:18
2017 Jul 31 21:41:20–21:42:12	2019 Sep 5 21:11:33–21:13:44
2017 Jul 31 21:42:15–21:44:00	2019 Sep 6 04:24:30–04:26:00
2017 Aug 1 01:00:05–01:02:00	2019 Sep 6 04:36:20–04:39:00
2017 Aug 18 17:10:10–17:12:10	2019 Sep 9 01:16:00–01:18:40
2017 Aug 18 17:12:15–17:13:45	2019 Sep 9 01:55:20–01:58:20

ORCID iDs

Elena E. Grigorenko https://orcid.org/0000-0003-0670-4642

References

Angelopoulos, V., Baumjohann, W., Kennel, C. F., et al. 1992, JGR, 97, 4027
Angelopoulos, V., Kennel, C. F., Coroniti, F. V., et al. 1994, JGR, 99, 21257
Artemyev, A. V., Neishtadt, A. I., & Angelopoulos, V. 2022, JGR, 127, e2022JA030265
Balikhin, M. A., Runov, A., Walker, S. N., et al. 2014, JGR, 119, 6367
Baumjohann, W., Paschmann, G., & Lühr, H. 1990, JGR, 95, 3801
Borg, A. L., Øieroset, M., Phan, T. D., et al. 2005, GeoRL, 32, L19105
Breuillard, H., Le Contel, O., Retino, A., et al. 2016, GeoRL, 43, 7279
Burch, J. L., Moore, T. E., Torbert, R. B., & Giles, B. L. 2016, SSRv, 199, 5
Drake, J. F., Swisdak, M., Che, H., & Shay, M. A. 2006, Natur, 443, 553
Fairfield, D., Mukai, T., Brittnacher, M., et al. 1999, JGR, 104, 355
Fu, H., Grigorenko, E. E., Gabrielse, C., et al. 2020, ScChD, 63, 235
Fu, H. S., Khotyaintsev, Y. V., André, M., & Vaivads, A. 2011, GeoRL, 38, L16104
Fu, X. R., Lu, Q. M., & Wang, S. 2006, PhPl, 13, 012309
Fujimoto, K. 2014, GeoRL, 41, 2721
Fujimoto, K. 2017, AnGeo, 35, 885
Grigorenko, E. E., Dubyagin, S., Malykhin, A. Y., et al. 2018, GeoRL, 45, 602
Grigorenko, E. E., Kronberg, E. A., Daly, P. W., et al. 2016, JGR, 121, 9985
Grigorenko, E. E., Malykhin, A. Y., Shklyar, D. R., et al. 2020, JGR, 125, e2020JA028268
Grigorenko, E. E., Sauvaud, J.-A., Palin, L., Jacquey, C., & Zelenyi, L. M. 2014, JGR, 119, 6553
Guo, Z. Z., Fu, H. S., Cao, J. B., et al. 2021, JGR, 126, e2021JA029900
He, R. J., Fu, H. S., Liu, Y. Y., Wang, Z., & Liu, C. M. 2021, GeoRL, 48, e2021GL096169
Hones, E. W., Jr. 1977, JGR, 82, 5633
Huang, S. Y., Jiang, K., Yuan, Z. G., et al. 2019, GeoRL, 46, 580
Huang, S. Y., Retino, A., Phan, T. D., et al. 2016, JGR, 121, 205
Huang, S. Y., Zhou, M., Deng, X. H., et al. 2012, AnGeo, 30, 97
Kennel, C. 1966, PhFl, 9, 2190
Khotyaintsev, Y. V., Cully, C. M., Vaivads, A., André, M., & Owen, C. J. 2011, PhRvL, 106, 165001
Kiehas, S. A., Runov, A., Angelopolos, V., Hietala, H., & Korovinksiy, D. 2018, JGR, 123, 1767
Lacombe, C., Alexandrova, O., Matteini, L., et al. 2014, ApJL, 790, L12
Le Contel, O., Leroy, P., Roux, A., et al. 2016, SSRv, 199, 257
Le Contel, O., Roux, A., Jacquey, C., et al. 2009, AnGeo, 27, 2259
Li, S.-S., Liu, J., Angelopoulos, V., et al. 2014, JGR, 119, 7181
Liang, J., Ni, B., Cully, C. M., et al. 2012, AnGeo, 30, 467
Liu, C. M., & Fu, H. S. 2019, ApJL, 873, L2
Liu, C. M., Fu, H. S., Xu, Y., et al. 2018, GeoRL, 45, 4628
Liu, J., Angelopoulos, V., Runov, A., & Zhou, X.-Z. 2014, JGR, 119, 909
Main, D., & Sotnikov, V. 2020, PhPl, 27, 022304
Malykhin, A. Y., Grigorenko, E. E., Shklyar, D. R., et al. 2021, JGR, 126, e2021JA029440
Merkin, V. G., Panov, E. V., Sorathia, K., & Ukhorskiy, A. Y. 2019, JGR, 124, 8647
Mishin, E., Sotnikov, V., Gerhenzon, N., & Sharma, A. 2019, GeoRL, 46, 7131e7136
Nagai, T., Fujimoto, M., Saito, Y., et al. 1998, JGR, 103, 4419
Nakamura, R., Baumjohann, W., Klecker, B., et al. 2002, GeoRL, 29, 1942
Nakamura, R., Varsani, A., Genestreti, K. J., et al. 2018, JGR, 123, 1260
Ohtani, S., Takahashi, K., Zanetti, L. J., Potemra, T. A., & Iijima, T. 1992, JGR, 97, 19
Oka, M., Phan, T. D., Krucker, S., Fujimoto, M., & Shinohara, I. 2010, ApJ, 714, 915
Panov, E. V., Artemyev, A. V., Baumjohann, W., Nakamura, R., & Angelopoulos, V. 2013, JGR, 118, 3065
Pickett, J. S. 2021, JGR, 126, e2021JA029548
Pollock, C., Moore, T., Jacques, A., et al. 2016, SSRv, 199, 331
Robert, P., Dunlop, M. W., Roux, A., & Chanteur, G. 1998, in Analysis Methods for Multi-spacecraft Data, ed. G. Pashmann & P. W. Daly (Noordwijk: ESA Publication Division), 395
Runov, A., Angelopoulos, V., Sitnov, M. I., et al. 2009, GeoRL, 36, L14106
Runov, A., Nakamura, R., Baumjohann, W., et al. 2003, GeoRL, 30, 1579
Russell, C. T., Anderson, B. J., Baumjohann, W., et al. 2016, SSRv, 199, 189
Sagdeev, R. Z., & Shafranov, V. D. 1961, JETP, 12, 130
Sergeev, V., Angelopoulos, V., Apatenkov, S., et al. 2009, GeoRL, 36, L21105
Sergeev, V., Runov, A., Baumjohann, W., et al. 2004, GeoRL, 31, L05807
Sergeev, V. A., Angelopoulos, V., & Nakamura, R. 2012, GeoRL, 39, L05101
Shiokawa, K., Miyashita, Y., Shinohara, I., & Matsuoka, A. 2005, JGR, 110, A09219
Shklyar, D., & Matsumoto, H. 2009, SGeo, 30, 55
Shklyar, D. R. 2011, PhL, 375, 1583
Shklyar, D. R. 2017, JGR, 122, 640
Slavin, J. A., Lepping, R. P., Gjerloev, J., et al. 2003, JGR, 108, 1015
Sun, W. J., Slavin, J. A., Tian, A. M., et al. 2019, GeoRL, 46, 6168
Tenerani, A., Le Contel, O., Califano, F., et al. 2013, JGR, 118, 6072
Thorne, R. M., & Tsurutani, B. T. 1981, Natur, 293, 384
Tong, Y., Vasko, I. Y., Artemyev, A. V., Bale, S. D., & Mozer, F. S. 2019, ApJ, 878, 41
Trakhtengerts, V. Y., & Rycroft, M. J. 2008, Whistler and Alfvén Mode Cyclotron Masers in Space (Cambridge: Cambridge Univ. Press)
Vasko, I. Y., Krasnoselskikh, V., Tong, Y., et al. 2019, ApJL, 871, L29
Viberg, H., Khotyaintsev, Y. V., Vaivads, A., et al. 2014, JGR, 119, 2605
Wang, R., Lu, Q., Nakamura, R., et al. 2016, JGR, 121, 9473
Wei, X. H., Cao, J. B., Zhou, G. C., et al. 2007, JGR, 112, A10225
Zhang, X., Angelopoulos, V., Artemyev, A. V., & Liu, J. 2018, GeoRL, 45, 9380
Zhang, X., Angelopoulos, V., Artemyev, A. V., & Liu, J. 2019, GeoRL, 46, 11718
Zhang, X.-J., & Angelopoulos, V. 2014, JGR, 119, 2536
Zhang, Y., Matsumoto, H., & Kojima, H. 1999, JGR, 104, 28633
Zhao, M. J., Fu, H. S., Liu, C. M., et al. 2019, GeoRL, 46, 2390
Zhao, Y., Wang, R., & Lu, Q. 2016, JGR, 121, 10898